Evaluation of an Induction Machine's Differential High Frequency Inductance for Self-Sensing Control Considering Iron Saturation

Constantin Schepe and Bernd Ponick
Leibniz University Hannover, Institute for Drive Systems and Power Electronics, Germany
constantin.schepe@ial.uni-hannover.de

***Abstract*—The saturation-dependent anisotropy of an induction machine (IM) is not rotor fixed and therefore constitutes a disturbance factor, which limits the controllability at low speed if the machine is to be operated with a self-sensing control. This paper describes a method to evaluate the differential high frequency (HF) inductance, which considers the saturation-dependent anisotropy by using transient finite element analysis (FEA) simulations with and without an injected carrier signal (CS). The voltage and current responses to the CS are extracted by eliminating the intersections of the two simulations. This allows analyzing the differential HF inductance without any overlay of interfering influences. Furthermore, the HF field distribution is visualized, giving insights into the physical origin of the saturation-dependent anisotropy and enabling the investigation of measures to reduce it.**

***Index Terms*—Anisotropy, Induction Motor, Iron Saturation, Self-Sensing Control**

I. Introduction

Depending on the operating speed of an electrical machine, different methods are used for self-sensing control. Regarding the medium and higher speed ranges, methods that evaluate the electromotive force (EMF) are very suitable [1], [2]. At lower speeds, the fundamental harmonic of the EMF cannot be reliably differentiated from disturbance factors. Therefore, another method is needed [2].

Anisotropy-dependent methods make use of the rotor position dependency of the stator inductances. By evaluating the current response to an injected carrier signal (CS), the differential high frequency (HF) inductance of the CS can be obtained. This allows the position and speed of the rotor to be estimated [2]. HF means in this context the frequency of the CS, which is usually in the range of some kilohertz. A prerequisite for the use of an anisotropy-dependent method is that a sufficiently strong magnetic anisotropy is present in the rotor, such as in synchronous machines (SMs) with salient poles or interior permanent-magnets due to the change in magnetic permeance along the circumference [3]. Regarding induction machines (IMs), a geometric magnetic anisotropy is only present due to the rotor slots. Rotor slots can have negative effects on the operating behavior of the machine, such as generating acoustic noise emissions or torque ripples. To counteract this, design measures such as rotor skewing, a suitable choice of rotor and stator slot numbers, or stator winding pitching are generally used. However, these measures also reduce the magnetic anisotropy caused by the rotor slots [4]. Therefore, IMs do usually not have a sufficiently strong magnetic anisotropy as a result of their geometry.

Another effect causing magnetic anisotropy is the iron saturation. Regarding SMs with surface-mounted permanent magnets, the d-axis saturation caused by the magnets can be used for the position estimation of the rotor [5]. In SMs with interior permanent magnets, the geometry-dependent magnetic anisotropy is increased by the iron saturation. However, for both SM types, iron saturation of the q-axis, which increases with load, weakens the magnetic anisotropy [5], [6].
Concerning IMs, however, the saturation-dependent anisotropy constitutes a disturbance factor if the machine is under load, since the anisotropy is not rotor fixed but stator field fixed, as shown in [7] and also in this paper.

In [8], an additional magnetic anisotropy is introduced by having a damping coil in the rotor of an SM, resulting in an increased anisotropy. [9] uses the idea of an additional rotor winding for an IM, but assumes for simplicity that no saturation-dependent anisotropy is present. Iron saturation is mentioned as a reason for deviations from simulation results and as a limiting factor for the anisotropy-dependent self-sensing control. With consideration of iron saturation, it is possible to distinguish between the saturation-dependent and rotor-fixed anisotropies. This approach can be used to predict saturation-dependent control limits and to determine influences of the IM design on the saturation-dependent anisotropy.

In [10], a method is presented which evaluates the current response to a CS considering iron saturation. It thus can distinguish between rotor- and stator-fixed anisotropies. For this purpose, transient finite element analysis (FEA) with an injected CS is performed. In post-processing, the current response to the CS is extracted by a filter.

The method presented in this paper shows how to evaluate the differential HF inductance using FEA. It extends the method from [10] by adding a parallel simulation without an injected CS. This allows applying intersection elimination, so that filtering in post-processing is no longer necessary and the methodology is correspondingly simplified. In addition, while simulations are performed with slip frequency in [10], it is shown here that, by simulating at a higher speed, the simulation time can be shortened, while an equivalent result

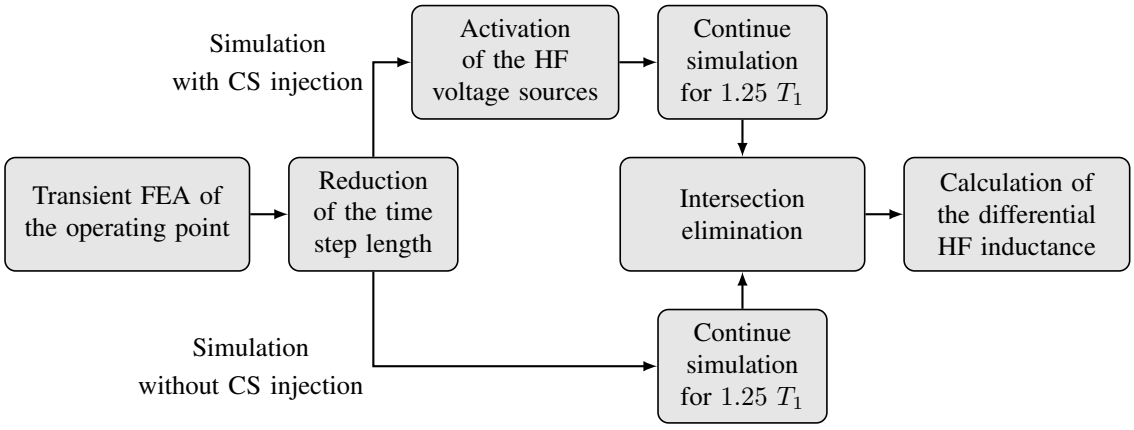

Fig. 1: Simulation workflow

is obtained. The simulation results are validated with measurements. Furthermore, it is shown that, due to the intersection elimination, the HF field distribution can be visualized. This provides information about how to design an IM with a reduced saturation-dependent anisotropy.

II. Methodology

A two-dimensional, transient, multi-slice, circuit-coupled FEA in time-stepping mode is used to simulate an operating point. The simulated IM is fed by three voltage sources in series with three additional HF voltage sources $u_{\mathrm{A,HF}}$, $u_{\mathrm{B,HF}}$, and $u_{\mathrm{C,HF}}$ applying the CS injection in the form of an alternating voltage vector

$$u_{\mathrm{A,HF}}\left(t\right) = \hat{u}_{\mathrm{c}} \cdot \sin\left(2\pi f_{\mathrm{c}} \cdot t\right) \tag{1}$$

$$u_{\mathrm{B,HF}}\left(t\right) = u_{\mathrm{C,HF}}\left(t\right) = 0.5 \cdot \hat{u}_{\mathrm{c}} \cdot \sin\left(2\pi f_{\mathrm{c}} \cdot t + \pi\right) \ , \tag{2}$$

with time represented by t, the CS voltage vector's amplitude by $\hat{u}_{\mathrm{c}}$ and the CS frequency by f_{c}.

The general simulation workflow is shown in Fig. 1. Starting with a constant speed, all currents equal to zero, and deactivated CS injection, the simulation is run until the steady state is reached. After this, the time step length is reduced, so that effects in the frequency domain of the CS can be taken into account. A time step length of one-eighth of the HF period has been found to provide a good compromise between accuracy and computation time. Next, the simulation is continued in parallel, once with and once without activated CS injection. The reduction of the time step length leads to a small transient response, which needs to have decayed before evaluating the last period. In this case, the steady state is reached after $0.25\ T_1$. Therefore, simulating another $1.25\ T_1$ is chosen to obtain a whole period of the fundamental frequency f_1 with and without CS injection.

Assuming that the CS has no significant effect on the IM's operating behavior, simulation results with the injected CS can be considered as a superposition of the operating behavior and the CS behavior. By intersection elimination, which means subtracting every state variable's result vector $\vec{x}$ in the simulation with CS injection from those obtained without, the resulting vectors then only contain parts excited by the CS injection

$$\vec{x}_{\mathrm{c}} = \vec{x}_{\text{with CS injection}} - \vec{x}_{\text{without CS injection}} \ . \tag{3}$$

As a consequence, filtering of the frequency domain as described in [10] is no longer needed, resulting in an output that is independent of the filter parameters.

To consider the anisotropy of each phase inductance in a single parameter, the differential HF inductance of the α-axis $L'_{\mathrm{c},\alpha}$ in the $\alpha\beta$ reference frame will be used in the following.

For the resulting CS current and voltage vectors, a discrete Fourier transformation (DFT) is employed to determine the time-dependent amplitudes $\hat{i}_{\mathrm{c},\alpha}\left(t\right)$ and $\hat{u}_{\mathrm{c},\alpha}\left(t\right)$ with frequency f_{c} as well as their phase angles $\varphi_{\,\mathrm{i_{c,\alpha}}}\left(t\right)$ and $\varphi_{\,\mathrm{u_{c,\alpha}}}\left(t\right)$. The DFT output vector is shortened compared to the input vector by the number of steps in one period T_{c}. Hence, to generate values for a whole period T_1, the input vector must contain the values for a time interval of length $T_1 + T_{\mathrm{c}}$. Finally, $L'_{\mathrm{c},\alpha}$ can be determined by

$$L'_{\mathrm{c},\alpha}\left(t\right) = \frac{\hat{u}_{\mathrm{c},\alpha}\left(t\right)}{\hat{i}_{\mathrm{c},\alpha}\left(t\right)} \cdot \frac{\sin\left(\varphi_{\,\mathrm{u_{c,\alpha}}}\left(t\right) - \varphi_{\,\mathrm{i_{c,\alpha}}}\left(t\right)\right)}{2\pi f_{\mathrm{c}}} \ . \tag{4}$$

A. Choice of the Simulated Speed

Although anisotropy-based methods for self-sensing control are only used for low speeds, it is useful in terms of computation time to perform the FEA simulation for a higher speed n and thus a higher frequency

$$f_1 = \frac{1}{T_1} = \frac{p \cdot n}{(1-s)} \ , \tag{5}$$

with p being the number of pole pairs and s the slip. Simulating at low speed results in a large ratio of T_1/T_{c}, meaning that a large number of CS periods must be simulated to map a complete period T_1 with CS injection. The number of time steps after reducing the time step length is given by

$$n_{\mathrm{steps}} = 1.25 \cdot \frac{T_1}{\frac{T_{\mathrm{c}}}{8}} = \frac{10 \cdot (1-s)}{p \cdot n \cdot T_{\mathrm{c}}} \ , \tag{6}$$

according to Section II. Neglecting slip, it can thus be assumed that the required number of time steps decreases linearly with increasing speed. Nevertheless, the condition $T_\mathrm{c} \gg T_1$ must be fulfilled so that the operating behavior of the IM is not affected.

For the evaluation of $L'_{\mathrm{c},\alpha}$, it is not the speed but instead the saturation state and the field-displacing effect of the rotor cage which are relevant. The saturation state is established according to the slot magnetomotive forces, which can be set identically for various f_1 according to the well-known ${}^{U}/_{f}$ scalar control characteristic [11]. The frequency of the CS injection remains unchanged, which means that the field-displacing effect concerning the CS frequency component is approximately the same.

Due to a small ${}^{T_1}/_{T_\mathrm{c}}$ ratio, the changes of the phase current and voltage within one CS period can no longer be neglected. However, intersection elimination also removes this influence, which ensures that it has no effect on the evaluation of $L'_{\mathrm{c},\alpha}$.

III. Experimental Results

To validate the simulation results, the differential HF inductance has been measured on a test bench at different operating points. The machine data of the IM used, which has a skewed squirrel cage rotor, are listed in Table I and a picture of the test bench, including the IM under investigation and a permanent magnet synchronous machine as a load machine, is shown in Fig. 2.

TABLE I: IM machine data

Rated terminal voltage	400 V
Rated phase current	15.4 A
Rated power	7.5 kW
Rated rotational speed	1479 min^{-1}
Number of pole pairs	2

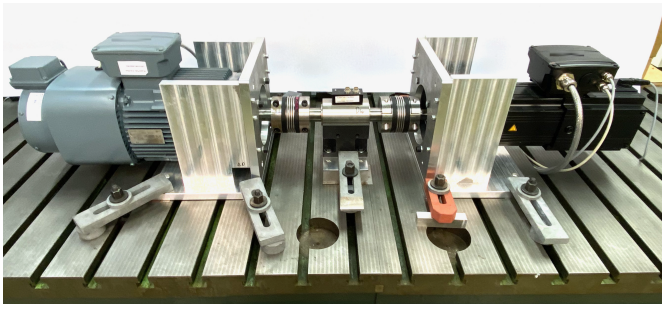

Fig. 2: Experimental test bench

A. Measurements

The d- and q-current values required for a field-oriented control are $i_\mathrm{d} = 10\,\mathrm{A}$ and $i_\mathrm{q} = 19.3\,\mathrm{A}$ for the rated operating point of the IM. The d_Ψ-axis of the rotating reference frame is oriented to the rotor flux Ψ'_R as it is described in [12] and as it is shown in Fig. 3. With constant i_d and a stepwise increase of i_q, measurements have been performed at a speed of 60 min^{-1}

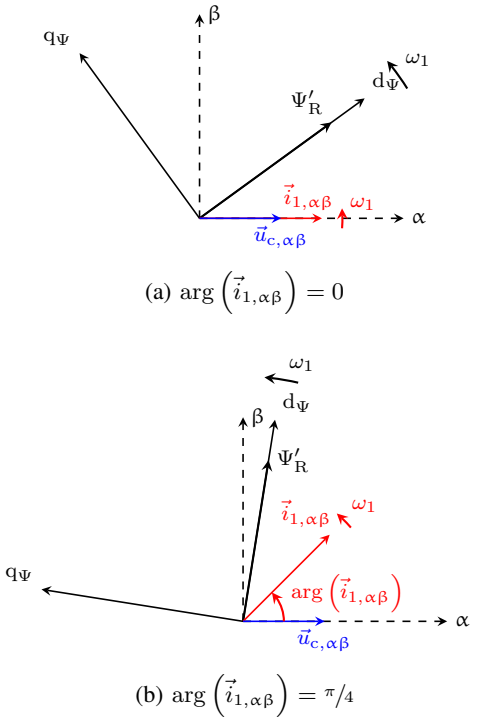

(a) $\arg\left(\vec{i}_{1,\alpha\beta}\right) = 0$

(b) $\arg\left(\vec{i}_{1,\alpha\beta}\right) = {}^{\pi}/_{4}$

Fig. 3: Phase current and CS vector in an αβ reference frame, with different positions of the stator current vector $\vec{i}_{1,\alpha\beta}$

from no-load ($i_\mathrm{q} = 0\,\mathrm{A}$) to $i_\mathrm{q} = 19.3\,\mathrm{A}$. The carrier signal is injected at a frequency of $f_\mathrm{c} = 4\,\mathrm{kHz}$ and an amplitude of $\hat{u}_\mathrm{c} = 40\,\mathrm{V}$. As shown in Fig. 3, the CS voltage vector $\vec{u}_{\mathrm{c},\alpha\beta}$ is located in the α-axis and the stator current vector $\vec{i}_{1,\alpha\beta}$ rotates with the electrical angular frequency ω_1. Since the IM has no rotor-fixed anisotropy, the instantaneous values of the measured inductance $L'_{\mathrm{c},\alpha}$ can thus be uniquely assigned to the argument of the stator current vector $\arg\left(\vec{i}_{1,\alpha\beta}\right)$.

B. Comparison of Measured and Simulated Results

The simulations have been performed with the rated frequency of 50 Hz to reduce the simulation time, as explained in Section II-A. The increased frequency leads to a reduction of the required time steps by a factor of ${}^{1500\,\mathrm{min}^{-1}}/_{60\,\mathrm{min}^{-1}} = 25$ in no-load operation and at least of 17.5 for the other operating points.

A comparison of the measured and simulated differential HF inductances plotted against the stator current vector's argument in αβ-coordinates is shown in Fig. 4. It can be seen that the simulated inductance generally matches well with the measured inductance for every operating point. Nevertheless, there are still some deviations. Regarding time harmonics, especially at no-load, the simulation shows a higher number of time harmonics or time harmonics with larger amplitudes than the measurement. This can be seen more precisely in the frequency spectrum of the harmonics shown in Fig. 5. In particular, the components at $4f_1$ and $8f_1$ are overestimated by the simulation. For no-load operation, these are negligibly small in the measured values. And for rated operation

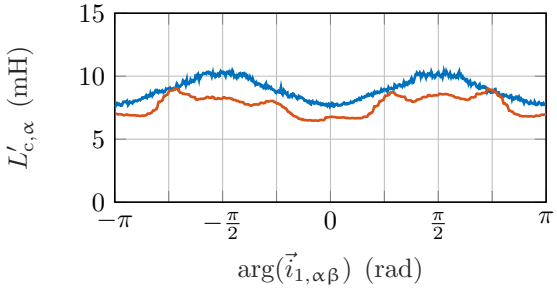

(a) $i_q = 0\,\mathrm{A}$

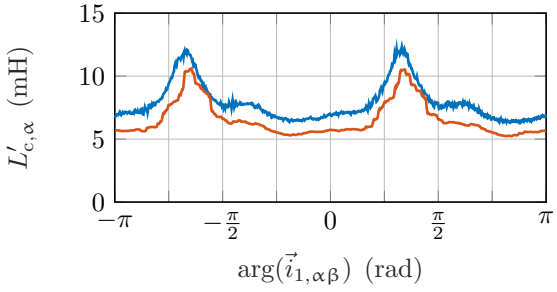

(b) $i_q = 6\,\mathrm{A}$

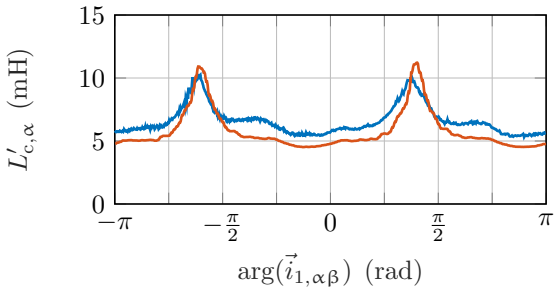

(c) $i_q = 12\,\mathrm{A}$

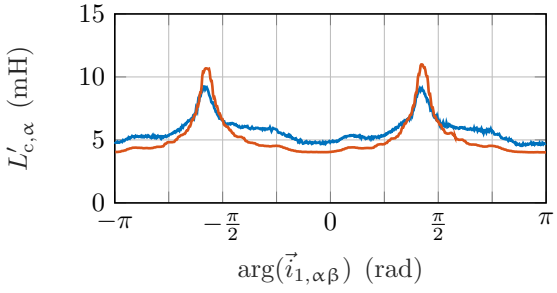

(d) $i_q = 19.3\,\mathrm{A}$

Fig. 4: Comparison of measured (blue) and the simulated (red) differential HF inductances $L'_{c,\alpha}$ using a symmetrical rotor

($i_q = 19.3\,\mathrm{A}$), the measurement for the components at $4f_1$ and $8f_1$ also shows significantly smaller amplitudes. Regarding other time harmonics, the simulated values are also higher than the measured values, but the progression of the amplitudes matches well. Thus, the damping of the higher time harmonics is not calculated correctly by the simulation. With $i_q > 0$, the measured maximum inductance value decreases with further increase of i_q, while the simulated value is almost constant.

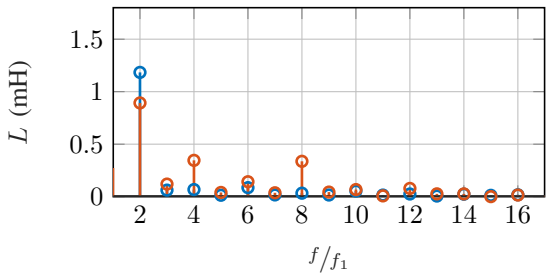

(a) $i_q = 0\,\mathrm{A}$

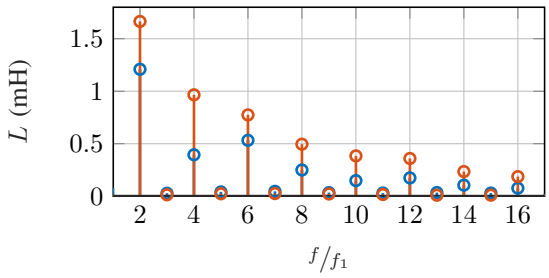

(b) $i_q = 19.3\,\mathrm{A}$

Fig. 5: Comparison of measured (blue) and simulated (red) time harmonics of $L'_{c,\alpha}$ using a symmetrical rotor

Furthermore, the minima of the simulated inductances are always below the measured values, which indicates that the magnetization curve used for the electrical sheet does not exactly match the sheet's characteristics. All in all, the method is shown to be well suited for the simulative determination of anisotropies.

C. Saturation-Dependent Anisotropy as a Disturbance Factor

In order to be able to evaluate the rotor position on the basis of an anisotropy, it must be rotor fixed. Existing non-rotor-fixed anisotropies do not contain any information about the rotor position and are therefore considered to be disturbance factors. The saturation-dependent anisotropy is an anisotropy caused by the main field in the machine. The main field and the resulting anisotropy move in the circumferential direction with the synchronous rotational speed

$$n_0 = \frac{f_1}{p}\,, \tag{7}$$

while the mechanical speed of the IM is

$$n = n_0\,(1 - s)\,. \tag{8}$$

Thus, the saturation-dependent anisotropy and a possible rotor-fixed anisotropy differ in terms of their rotational speed by the slip speed $n_0 \cdot s$.

In Fig. 6, the measured slip values are plotted against i_q and range from 0 to 0.3. In Fig. 7, the measured frequency spectrum of $L'_{c,\alpha}$ is shown for both no-load operation and rated operation. It can be seen that, independent of i_q and thus independent of the IM's slip, the fundamental frequency

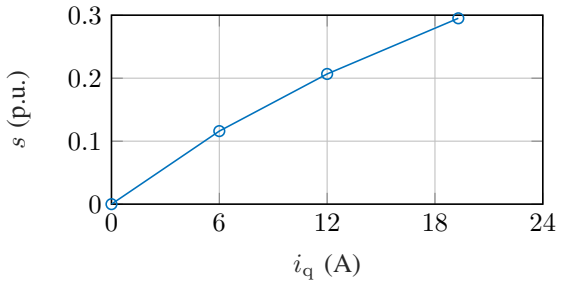

Fig. 6: Measured slip values from no-load to rated operation at $60\,\mathrm{min}^{-1}$

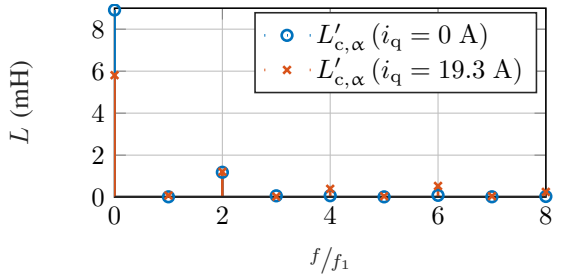

Fig. 7: Measured frequency spectrum of $L'_{\mathrm{c},\alpha}$ under no-load operation and rated operation using a symmetrical rotor

of the differential HF inductance is $2f_1$ and is therefore not rotor fixed.

IV. Discussion of Field Distribution

In order to take measures to reduce saturation-dependent anisotropy, it is important to understand the physical causes of it. Thus, in this section, an analysis of the field and flux density distribution is performed based on the simulation results.

Fig. 8 shows the field distribution and flux densities for the considered IM at the times of an inductance minimum and a maximum at rated torque (cf. Fig. 4d). The field distribution can be seen to be approximately independent of the rotor position. The main field, which dominates the field distribution in Fig. 8, can hence also be assumed to be independent of the rotor position.

By applying intersection elimination to the vector potentials of the field solutions, the component of the field resulting from the CS injection can be extracted. Flux paths relevant to the evaluation of $L'_{\mathrm{c},\alpha}$ can thus be visualized in Fig. 9. With simultaneous visualization of the total flux density, it is possible to show the influence of iron saturation on the flux excited by the CS.

In contrast to the field lines shown in Fig. 8, the field of the CS shown in Fig. 9 is displaced from the rotor cage due to its high frequency. Thus, the flux caused by the CS travels along the surface of the rotor. Therefore, the iron saturation of the rotor surface has a strong effect on the differential inductance $L'_{\mathrm{c},\alpha}$. In Fig. 10, coloration according to the flux density shows that the most saturated iron regions are present at the rotor surface. Furthermore, significant differences in saturation can be seen along the rotor surface.

Unlike the main field, which is a rotating field, the field excited by the CS is an alternating field with a spatially fixed axis. In contrast, the main field moves with n_0 around the circumference (cf. Fig. 8 and Fig. 9). The iron saturation depends on the main field and shows a maximum and a minimum for each pole. Hence, during an electrical period of the fundamental frequency, two saturation minima and two saturation maxima pass through the stator-fixed α-axis, which is also the axis of the CS field. Thus, the magnitude of $L'_{\mathrm{c},\alpha}$ is affected by the angular difference between the axis of the main field and that of the CS field. The two extrema are shown in Fig. 9 and Fig. 10. At the maximum of $L'_{\mathrm{c},\alpha}$, the most saturated region of the rotor surface is close to the α-axis. The field excited by the carrier signal is mostly concentrated in unsaturated regions at this time, which maximizes $L'_{\mathrm{c},\alpha}$. If the most saturated region of the rotor surface is near the β-axis, the field cannot form exclusively in the unsaturated regions and $L'_{\mathrm{c},\alpha}$ becomes minimal.

In order to reduce the saturation-dependent anisotropy, the leakage flux paths and, above all, the rotor surface should be designed to be as independent of saturation as possible. A significant influence can be expected if the rotor slots are open to the air gap instead of closed, as is the case here. This would reduce the magnetic permeance at the rotor surface and the difference in magnetic permeance in the saturated and unsaturated regions would be less noticeable. In [13], it is shown that the number of rotor slots and the selected stator winding pitching have significant influences on the flux leakage. By further investigating the influence of other parameters, such as the stator and rotor slot opening widths, design recommendations can be developed to minimize saturation-dependent anisotropy. The addition of a dominant rotor-fixed anisotropy is facilitated by these measures.

V. Conclusion

A method to simulate the differential high frequency inductance of an IM by using transient FEA has been demonstrated. The novel approach uses parallel simulations with and without the injection of a CS followed by intersection elimination. This allows separate evaluations of the current and voltage responses excited by the carrier signal without interfering influences. Furthermore, performing the simulation with an increased speed but with an equivalent saturation level reduces the computation time by a factor of at least 17.5. The simulation results match well with the measurements.

By illustrating the field distribution excited by the carrier signal and also the saturation state caused by the main field, the properties of saturation-dependent anisotropy as a disturbance and its physical origin are explained.

Acknowledgment

This work was funded by the Deutsche Forschungsgemeinschaft (DFG, German Research Foundation), project identification number 424944120.

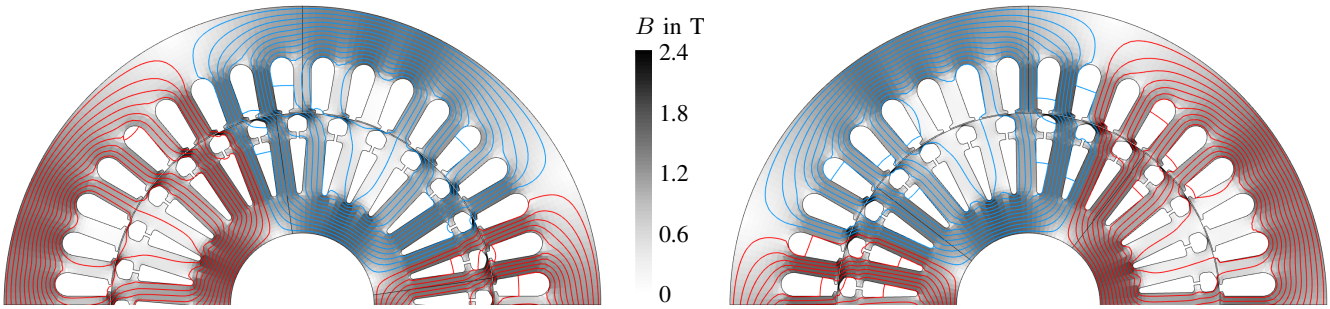

(a) $\min\left(L'_{\mathrm{c},\alpha}\left(i_\mathrm{q}=19.3\,\mathrm{A}\right)\right)$ (b) $\max\left(L'_{\mathrm{c},\alpha}\left(i_\mathrm{q}=19.3\,\mathrm{A}\right)\right)$

Fig. 8: Overall field lines and overall flux density distribution at rated operation, respectively at the times of minimum and of maximum of $L'_{\mathrm{c},\alpha}$

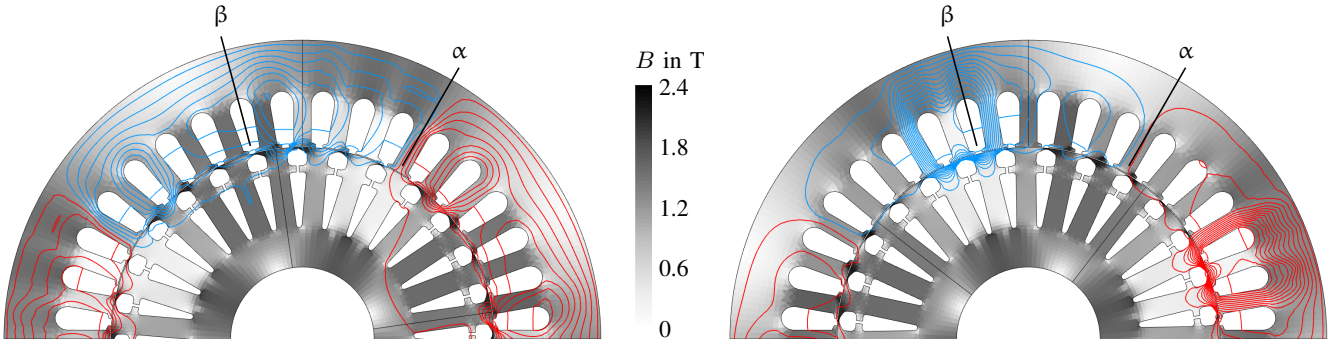

(a) $\min\left(L'_{\mathrm{c},\alpha}\left(i_\mathrm{q}=19.3\,\mathrm{A}\right)\right)$ (b) $\max\left(L'_{\mathrm{c},\alpha}\left(i_\mathrm{q}=19.3\,\mathrm{A}\right)\right)$

Fig. 9: Field lines excited by the CS and overall flux density distribution at rated operation, respectively at the times of minimum and of maximum of $L'_{\mathrm{c},\alpha}$

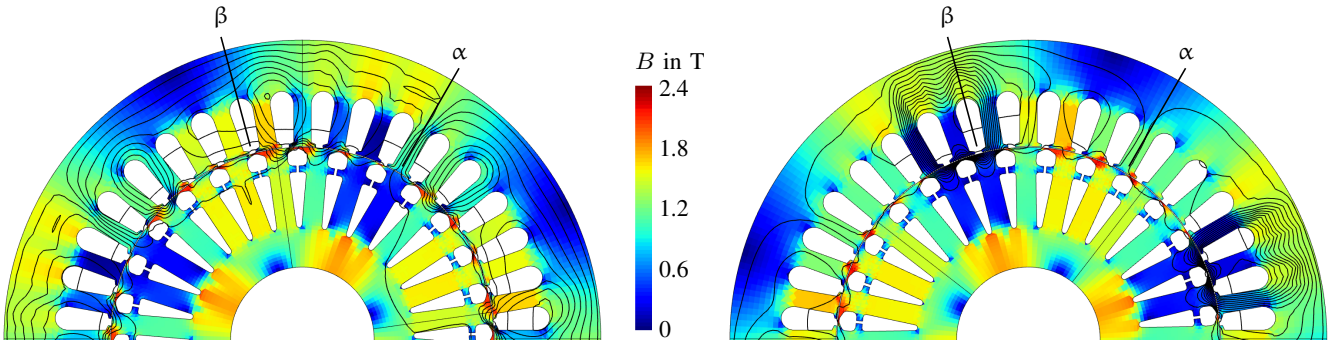

(a) $\min\left(L'_{\mathrm{c},\alpha}\left(i_\mathrm{q}=19.3\,\mathrm{A}\right)\right)$ (b) $\max\left(L'_{\mathrm{c},\alpha}\left(i_\mathrm{q}=19.3\,\mathrm{A}\right)\right)$

Fig. 10: Field lines excited by the CS and overall flux density distribution (in iron parts only) at rated operation, respectively at the times of minimum and of maximum of $L'_{\mathrm{c},\alpha}$

References

[1] J. Holtz, "Sensorless control of induction motor drives," *Proceedings of the IEEE*, vol. 90, no. 8, pp. 1359–1394, Aug 2002.

[2] D. Schröder and J. Böcker, *Elektrische Antriebe - Regelung von Antriebssystemen*. Springer, 2015, vol. 4, ch. 15, pp. 943–973.

[3] I. Hahn, "Differential magnetic anisotropy - prerequisite for rotor position detection of pm-synchronous machines with signal injection methods," in *2010 First Symposium on Sensorless Control for Electrical Drives*, July 2010, pp. 40–49.

[4] M. A. Samonig and T. M. Wolbank, "Prediction of slotting saliency in induction machines with respect to high-frequency-excitation based sensorless control," in *IECON 2014 - 40th Annual Conference of the IEEE Industrial Electronics Society*, Oct 2014, pp. 794–799.

[5] R. Kennel, "Encoderless control of synchronous machines with permanent magnets - impact of magnetic design," in *2010 12th International Conference on Optimization of Electrical and Electronic Equipment*, May 2010, pp. 19–24.

[6] N. Bianchi, E. Fornasiero, and S. Bolognani, "Effect of stator and rotor saturation on sensorless rotor position detection," *IEEE Transactions on Industry Applications*, vol. 49, no. 3, pp. 1333–1342, May 2013.

[7] I. P. Brown and R. D. Lorenz, "Induction machine design methodology for self-sensing: Balancing saliencies and power conversion properties," *IEEE Transactions on Industry Applications*, vol. 47, no. 1, pp. 79–87, Jan 2011.

[8] F. Quattrone and B. Ponick, "Evaluation of a permanent magnet synchronous machine with a rotor coil for improved self-sensing performance at low speed," in *2016 XXII International Conference on*

Electrical Machines (ICEM), Sep. 2016, pp. 1680–1685.

[9] S. Luecke and A. Mertens, "Self-sensing design and control for an induction machine with an additional short-circuited rotor coil," in *2022 24th European Conference on Power Electronics and Applications (EPE'22 ECCE Europe)*, Sep. 2022, pp. 1–9.

[10] I. P. Brown and R. D. Lorenz, "Response surface methodologies for the design of induction machine self-sensing rotor position saliencies," in *2007 International Conference on Electrical Machines and Systems (ICEMS)*, Oct 2007, pp. 1354–1359.

[11] I. Boldea and S. A. Nasar, *The induction machine handbook*. CRC press, 2001, ch. 8, pp. 243–248.

[12] W. Leonhard, *Control of Electical Drives*, 3rd ed. Springer-Verlag Berlin Heidelberg, 2001, ch. 12, pp. 252–259.

[13] M. A. Samonig and T. M. Wolbank, "Analyzing the influence of induction machine design on transient slot leakage inductance with respect to sensorless rotor position estimation," in *2017 IEEE International Electric Machines and Drives Conference (IEMDC)*, May 2017, pp. 1–6.